Proceedings of ASME Turbo Expo 2011
IGTI 2011
June 6-10, 2011, Vancouver, Canada

GT2011-46548

NOISE PREDICTION OF PRESSURE-MISMATCHED JETS USING UNSTRUCTURED LARGE EDDY SIMULATION

Yaser Khalighi*, Frank Ham, Parviz Moin
Cascade Technologies Inc.
Palo Alto, CA 94303

Sanjiva K. Lele
Dept. Mechanical Engineering
Stanford University
Stanford, CA 94305

Robert Schlinker, Ramons Reba, John Simonich
United Technologies Research Center
411 Silver Lane
East Hartford, CT 06108

1 Introduction

The noise environment associated with take-offs and landings of a combat aircraft on an aircraft carrier deck is one of the loudest sources of aerodynamically generated sound. Noise levels at 50 feet from the take-off point of the aircraft are reported to be in the range of 140-152 dB. Exposure to these intense noise levels can cause permanent damage to hearing and result in other severe adverse health impacts. According to NRAC report (2009), it has been estimated that in the US military the disability claims associated with hearing loss exceed $1 B each year. Finding effective strategies to mitigate the exposure to the severe noise associated with the operations of combat aircraft are critical. Similarly strategies which significantly reduce the noise intensity at the source without severely impacting propulsive performance, and which significantly reduce the noise footprint (in intensity and in terms of the affected area) are required. As discussed below the complexities of the flow responsible for this intense noise generation are very difficult to model using semi-empirical prediction methods. However, recent advances in computer hardware and numerical algorithms have now enabled a first-principles approach, called large-eddy simulation (LES), to the aeroacoustic prediction of propulsive jets.

The propulsion systems of combat aircraft are based on low-bypass ratio turbo-jet engines. The exhaust jets are hot (gas temperature exceeding 1000 deg F) and are supersonic. The jet flow is surrounded by a turbulent shear layer, which entrains the ambient air into the jet flow and mixes with it. The shear-layer turbulence contains quasi-organized coherent structures as well as broadband turbulent fluctuations. These organized structures and turbulent eddies move with the jet flow at a supersonic speed relative to the still ambient air. This process is akin to that of a supersonically moving bullet/projectile and launches a local "sonic boom" associated with each organized structure or turbulent eddy. Additional intense noise emissions arise from the region downstream where the jet potential core breaks down and mixes vigorously and intermittently with the ambient cooler air. These processes generate intense turbulent mixing noise, which radiates preferentially at shallow angles to the jet axis. The ground personnel on aircraft carrier deck are directly exposed to this dominant supersonic jet noise radiation. Particular to combat aircraft is the operation of afterburner in the engine. It is designed to increase the propulsive thrust of the engine by increasing the stagnation temperature of the propulsive stream by additional burning of fuel. Increased thrust is associated with increased jet exhaust velocity, which further increases the jet noise. The additional trust causes a mismatch in pressure between the exhaust stream and the ambient. This pressure mismatch generates a complex train of shock-cells within the jet plume, which interacts with the jet turbulence. This gives rise to additional noise: tonal emission called jet screech and the broadband shock-associated noise (BBSN). Both radiate preferentially towards the inlet of the aircraft.

Existing engineering methods for estimating the noise of propulsive jets and its interaction with the ground rely heavily on empirical databases developed using scaled model testing and the available full-scale data. While these semi-empirical methods provide useful first estimates they lack the sensitivity to design/configuration changes needed in a design tool to usefully evaluate the benefits and drawbacks of various strategies for mit-

*email: khalighi@cascadetechnologies.com

igating the noise exposure to the aircraft carrier deck personnel. An LES based prediction method, which captures the physics of the various relevant aerodynamic noise generation processes and their interactions while dealing with the realistic geometrical configurations is now feasible. By capturing the unsteady flow physics responsible for the noise-generation, LES provides a first-principles approach to understand the crucial contributors to supersonic jet aeroacoustics, and to evaluate various strategies for mitigating the noise impacts. This physics-based approach is free of user-defined models or parameters or empirical constants. However, its predictive capability centrally depends on adequate capturing of the unsteady flow phenomena responsible for noise generation. In high-Reynolds number complex turbulent flows this requires a careful design of the mesh to capture the noise-source dynamics directly and thus LES requires substantially more computer resources than a steady state RANS calculation. It should be underscored that attempts by many groups at predicting the noise of high-speed turbulent jets using LES has had mixed success (Ladeinde *et al.*, 2008; Lo *et al.*, 2008). As reviewed by Bodony & Lele (2008), numerical dissipation, inadequate azimuthal resolution, and artificially thick near-nozzle shear layers contributed to poor predictions.

Cascade Technologies has developed a general LES framework (known as CharLES) for compressible turbulent flows and noise predictions. In such framework the nozzle geometry directly influences the turbulent flow inducing its coherent and fine-scale motions, and the effect of propulsion system design choices can be logically addressed. The novel features of this framework include its emphasis on low-dissipation and dispersion numerical discretization on unstructured meshes, localized adaptive refinement to capture fine-scale turbulence, localized shock-capturing and careful verification and validation efforts for jet flows under a variety of operating conditions. A description of this technology was previously presented by Khalighi *et al.* (2010). In that work, CharLES was applied to predict the flow and noise issued by a perfectly expanded supersonic nozzle. In practical application, nozzles do not operate in perfectly-expanded conditions; the static pressure at the exit of the supersonic nozzle is generally not matched with the ambient pressure. The pressure mismatch generates a shock cell system that interacts with the turbulence and cause additional noise components. In addition, the interaction of shock cells and turbulent plume plays a significant role in the mechanism of noise generated by a jet impinging on a jet blast deflector (JBD) or on ground in short takeoff and vertical landing (STOVL) vehicles.

A high fidelity LES tool suitable for capturing shock/turbulence interaction requires a careful implementation of the shock-capturing scheme; in one hand, it is known that excessive numerical dissipation has a detrimental effect on the quality of turbulent flow solution and sound obtained from LES; in other hand, local numerical dissipation is required to capture strong shocks in the flow (Mani *et al.*, 2009). In this work we will present the implementation of the shock-capturing method in CharLES and demonstrate the application of our method to a variety of pressure-mismatched jets. In addition, grid-sensitivity study for an unheated jet issued from a round nozzle will be presented; this is the continuation of validation study presented by Khalighi *et al.* (2010).

Here we first present the unstructured LES solver, in particular, shock-capturing scheme, next we present the mesh refinement study of an isothermal, ideally-expanded supersonic jet, then we demonstrate flow and sound calculations of free and impinging jets under pressure-mismatched conditions. For impinging jets, we consider impingement on a JBD as well as on ground for STOVL aircrafts.

2 Unstructured LES and shock capturing

CharLES solves the spatially-filtered compressible Navier-Stokes equations in finite volume form using the following control-volume (cv) based discretization:

$$\frac{\partial U}{\partial t} V_{cv} + \sum_f \left(F^e + F^d \right) A_f = S V_{cv} \tag{1}$$

where $U = [\rho, \rho u, \rho v, \rho w, \rho E]^T$ is the vector of conserved variables representing the average state in the control volume, V_{cv} is the constant cv volume, F^e and F^d are the face-normal inviscid (Euler) and diffusive fluxes respectively, A_f is the face area, and S is the source vector.

2.1 Euler flux F^e

The Euler flux at each face is computed using the following two-step approach:

1. polynomial reconstruction of left and right-biased data to the face centroid, followed by
2. flux computation using a mix of centered and upwind-biased Riemann flux based on the biased reconstructed data.

Both of these steps are now described in detail.

2.2 Biased Polynomial Reconstruction to the Face Centroid

Consider the reconstruction of an arbitrary cv-based scalar ϕ at an internal face f associated with a left (L) and right (R) control volume as shown in figure 1. When the ϕ solution is considered smooth, the left (l) and right (r) biased data is reconstructed at the face centroid using the following relations:

$$\phi_l = \phi_L + a_l(\phi_R - \phi_L) + b_l \cdot \nabla \phi_L \tag{2}$$

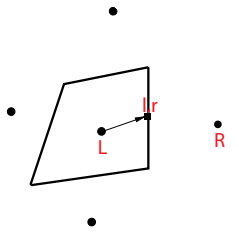

Figure 1. 2D schematic of a control volume and its neighbors illustrating the left and right convention associated with a given face.

$$\phi_r = \phi_R + a_r(\phi_L - \phi_R) + b_r \cdot \nabla\phi_R \tag{3}$$

where $\nabla\phi_L$ and $\nabla\phi_R$ are second-order gradients associated with the left and right cvs, and a_l, a_r, b_l, and b_r are pre-computed reconstruction coefficients associated with each face. These coefficients depend on the local geometry such that the reconstructed value at the face recovers the highest possible polynomial accuracy (maximum 3^{rd}-order) while still remaining sufficiently biased to allow upwinding to introduce dissipation.

For example, on a regular, orthogonal Cartesian grid with uniform cell size h at a face in the x-direction, these coefficients take on the following values:

$$a_l = \frac{1}{6}, \quad a_r = \frac{1}{6}, \quad b_l = \frac{1}{3}[h,0,0], \quad b_r = \frac{1}{3}[-h,0,0] \tag{4}$$

It is instructive to simplify this reconstruction in terms of the cv labels shown in figure 2.

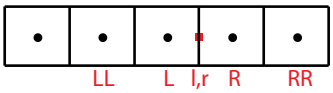

Figure 2. 2D schematic of structured Cartesian control volumes surrounding a given face.

Using the following definition for the x-gradient in the left cv,

$$\left.\frac{\partial\phi}{\partial x}\right|_L = (\phi_R - \phi_{LL})/2h \tag{5}$$

equation 2 simplifies to the following quadratic polynomial:

$$\phi_l = -\frac{1}{6}\phi_{LL} + \frac{5}{6}\phi_L + \frac{1}{3}\phi_R \tag{6}$$

In practice, this simplification is never used because no assumptions are made about the regularity of the grid. However, the method is equivalent to a structured method when the grid becomes locally Cartesian and uniform.

In the reconstruction phase, the above procedure is used to compute left and right-biased values at all internal faces for the primitive variables ρ, p, and u_i. Numerical experiments were conducted to test whether alternative descriptions of the state (e.g. the conserved variables) could be reconstructed, however this primitive description of the state was the most robust.

2.3 Euler flux computation using a mix of centered and upwind-biased Riemann flux

The Euler flux is computed at each control volume face using a blend of a non-dissipative central flux and a dissipative upwind flux:

$$F^e = (1-\alpha)F^{central} + \alpha F^{upwind} \tag{7}$$

where $0 \leq \alpha \leq 1$ is a blending parameter. This blending approach is often the basis of implicit approaches to LES, where the blending parameter is selected as a global constant with a value large enough to provide all the necessary dissipation (and potentially quite a bit more). For example, in the turbulent jet literature Tucker Tucker (2004) used this approach and reported that the smallest "usable" value of blending parameter was determined to be $\alpha = 0.25$. The treatment is described in detail by Shur *et al.* Shur *et al.* (2003). In later work, Xia and Tucker Xia *et al.* (2009) reported that the minimum value of blending parameter was set to 0.1 "to avoid numerical instability".

CharLES does *not* use the implicit LES approach – an explicit sub-grid scale model is used to model the effect of sub-grid scales (see next section). To minimize numerical dissipation relative to implicit LES approaches, the value α is allowed to vary spatially such that it can be set to zero in regions where the grid quality is good and the scheme based on the central flux is linearly stable and non-dissipative. In regions of less-than-perfect grid quality, however, the central scheme can introduce numerical instabilities that must be prevented from contaminating/destabilizing the solution by locally increasing α. The novel aspect of CharLES is its algorithm to compute this locally optimal α based on the properties of the differencing operator. This algorithm is described in Khalighi *et al.* (2010).

2.4 Shock-capturing

Shocks, like sub-grid scale turbulence, are sub-grid phenomena and thus require modeling to account for their effect on the resolved flow. Unlike sub-grid scale turbulence, however, they are localized in the flow, and a surgical introduction of modeling is potentially more appropriate. CharLES uses a hybrid Central-ENO scheme to simulate flows involving shocks. The scheme has three pieces:

1. A central scheme, described previously
2. An scheme appropriate for computing a flux across a shock,
3. A hybrid switch, which detects where shocks are present in the flow, and activates the shock-appropriate scheme.

For the shock-appropriate scheme, CharLES uses a 2nd-order ENO method to perform left and right biased reconstructions. Because the ENO stencils are linear, the "smoothness" by which the different stencils must be compared is simply the difference between the reconstructed face value and the upwind cv value. Thus ENO can be implemented very efficiently without ever having to compute or store the smoothness associated with each stencil.

There are a number of different hybrid switches available to activate the shock-capturing scheme where required. One of the most robust is to activate the scheme when the reconstructed value of pressure or density at the face differs by more than some fraction of the local pressure or density. This is called "relative solution" or RS switch, and values of 0.1 to 0.2 seem to work effectively, controlling the oscillations near shocks, and turning off in other regions of the flow. Note that smaller values will lead to more shock capturing, with zero producing shock-capturing everywhere. This relative smoothness test is applied to both density and pressure because they are quantities that must be positive. By making the actual threshold a fraction of the local solution value, this tends to apply more shock capturing where the local density and/or pressure is near zero, naturally adding robustness to the approach.

In some cases, such as the pressure mismatched jet shown in figure 3 (see Section §4), the relative solution approach alone leads to stable solutions that still show oscillations near the shocks. It is possible to add additional shock-capturing to control this oscillation using a switch based on dilatation, while still allowing the shear layer to transition quickly out of the nozzle.

3 Fine-resolution simulation of a pressure-matched isothermal jet

In this section, we report the results of a high resolution simulation of flow and noise of a pressure-matched supersonic nozzle. It should be underscored that in this case only residual and weak shocks are present and the shock-capturing scheme introduced above is not active. Results presented in this section is a grid-refinement study and the continuation of our previous work (Khalighi *et al.*, 2010).

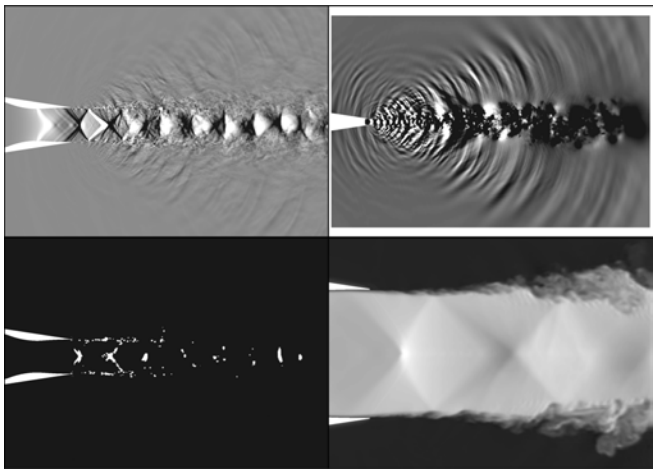

Figure 3. Pressure mismatched jet simulation: top left) dillitation; top right) pressure; bottom left) hybrid switch; bottom right) temperature near nozzle lip.

The computation model were designed to reproduce unheated jet B118 conditions tested at UTRC's acoustic research tunnel facility. The exit Mach number of $M_j = 1.5$ and jet exit static to chamber static temperature ratio is $T_r = 1.0$. The jet exhausts into an anechoic chamber which is subject to a wind tunnel flow with Mach number of $M_t = 0.1$. The Reynolds number for the unheated jet based on the jet exit velocity, jet diameter, and viscosity at the nozzle exit is 2×10^6. The ART jet is surrounded by a forward flight open jet wind tunnel which exhausts into an anechoic chamber. The open jet velocity was set to a Mach number of $M_t = 0.1$ to avoid overheating the anechoic chamber. The same $M_t = 0.1$ free stream flow condition was used in the computational simulation. A coarse and medium LES computation for this jet was carried out earlier by Khalighi *et al.* (2010). The number of grid cells in coarse and medium meshes are 11 million and 13 million, respectively.

The computational domain for this problem is shown in figure 4. As shown in this figure, a sponge layer is applied at the outlet of computational domain by applying a damping function as a source term in the NS equations. By using this method, the turbulent structures and sound waves will be damped before approaching the outlet boundary. The sponge layer is designed based on the method of Mani (2010). The acoustic projection surface for computing the far-field sound is also shown in this figure. To avoid the spurious noise sue to the closure of acoustic projection method, the method introduced by Shur *et al.* (2005) is applied; 15 end-caps spanning from $x = 20D$ to $x = 30D$ are used to eliminate the uncorrelated (erroneous) sound.

Figure 5 demonstrates two sets of LES prediction stations corresponding to UTRCs experimental set up in which near-field

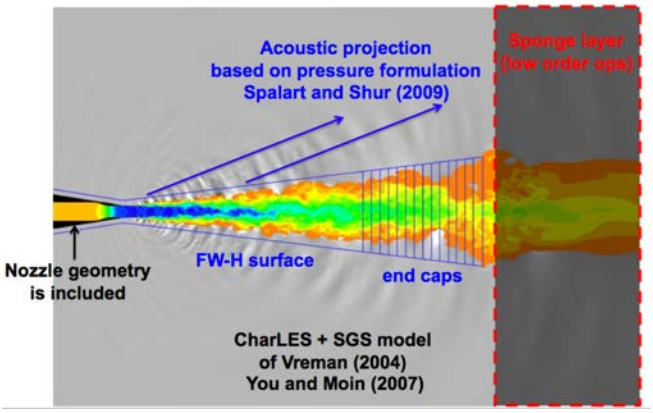

Figure 4. LES computational domain. Axial velocity field is shown in color, pressure is shown in grayscale.

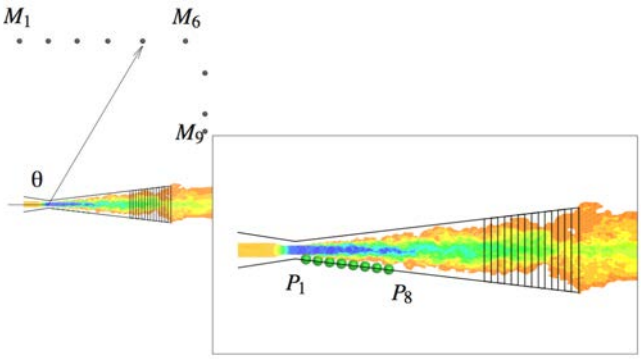

Figure 5. FWH surface and two sets of microphones used for calculation of noise; P_1 - P_8 are nearfield pressure probes; M_1 - M_9 are farfield microphones.

and far-field microphones were used as reported by Schlinker *et al.* (2008). The near-field probes and far-field microphones are annotated as $P_1 - P_8$ and $M_1 - M_9$, respectively.

The new refined mesh used in this study (known as 118F) consists of 42 M unstructured grid cells. The topology of the mesh, in particular, the azimuthal refinement, is similar to that of mesh 118M of Khalighi *et al.* (2010). The main differences of 118F and 118M are:

1. The ratio of radial and axial mesh-size in the bulk of the mesh within the FWH surface is close to unity. This ratio was approximately 1/2 in 118M.
2. The radial and axial resolution are selected such that waves with wavelength corresponding to $St = 6$ are resolved with 5 grid points per wavelength.
3. In 118F, the number of azimuthal grid points is 160 in the bulk of the mesh. The number of azimuthal grid points was 128 in 118M.

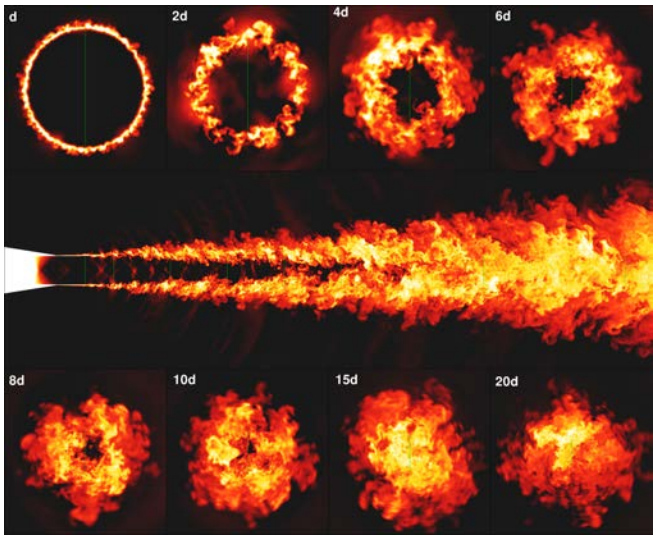

Figure 6. Temperature field for B118 (simulation 118F). The axial cuts of temperature are shown in top and bottom subfigures. The darkest and lightest colors show T_0 and $1.1T_0$, respectively. T_0 is the atmospheric temperature.

An instantaneous snapshot of temperature field is shown in figure 6. This plot clearly shows more crisp and detailed turbulent structures than simulation 118M. According to this figure, the thin laminar shear layer issued from the nozzle transitions to turbulence within one diameter from the nozzle exit. The turbulent flow mixes at the farther distance downstream of the nozzle. Mach wave radiation of sound initiated from the onset of mixing layer is also visible in the temperature field. A better visualization of sound waves are shown in figure 7. The dominant noise radiation towards aft angles is clearly visible; this radiation is mainly initiated from the vicinity of the nozzle exit. Smaller amount of acoustic energy is radiated in other directions and the source appears to be farther downstream within the jet plume. It should be underscored that pressure waves far from the jet plume (and the FWH surface) are captured using a coarse mesh. As a result, the visualized sound waves does not represent the actual computed sound using FWH surface method. We have visualized the sound waves computed using FWH and compared it to the directly computed sound in a different jet (not presented here), the visualized sound field using FWH exhibits much richer wavenumber content in the sound field in the regions far from the jet plume.

The simulation started from a solution obtained from 118M mesh interpolated on 118F. After simulation reaches statistical convergence, flow statistics were collected for 130 nondimentional time units. Time is non-dimensionalized by centerline jet velocity and jet diameter at nozzle exit. Figures 8 demonstrates the mean and r.m.s. of the axial velocity on the centerline of the jet. According to this figure, the jet centerline velocity

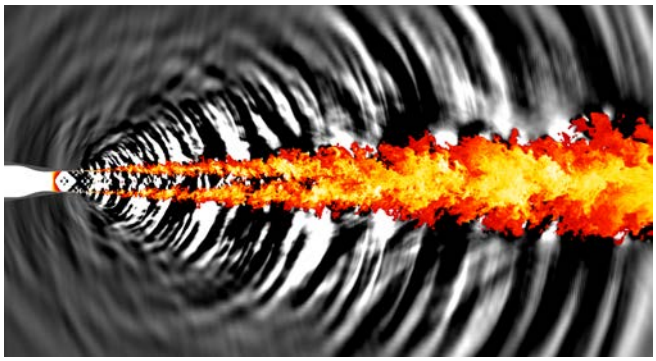

Figure 7. Temperature and pressure field for B118 (simulation 118F) shown in redscale and grayscale, respectively.

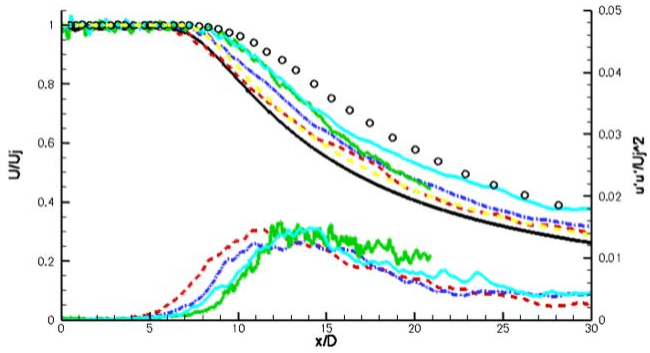

Figure 8. Comparison of mean and r.m.s. axial velocity for unheated jet; ——— , RANS; cyan, LES(118F), blue, LES(118M); red, LES(118C); green, measurement of Bridges & Wernet (2008) for $M_j = 1.4$; ○ , UTRC measurements for $M_j = 1.5$; yellow, predictions based on correlations of Witze (1974).

is consistently converging toward the UTRC's measurement by refining the simulation.

Figures 9 shows the near-field sound spectra for 118M and 118F and a comparison to experimental measurements. Near-field probe stations at which the comparison are performed are shown in figure 5. To achieve better statistical convergence, the pressure spectra was averaged on 48 near-field probes equally-spaces in azimuthal direction. The agreement of fine simulation (118F) and measurement is excellent. The convergence of solution toward the experimental measurements by mesh refinement is clearly visible; the higher levels of pressure at high frequencies predicted by medium resolution LES at P_5 and P_7 indicates the lack of resolution at these regions. As a result, the energy associated with these structures appear as numerical noise and contaminate the solution at higher frequencies. This numerical artifact is not present in the fine simulation. As previously discussed by Khalighi *et al.* (2010), the low frequency peaks at P_1 that appear in both LES and the UTRC experiment is hypothesized to be vortex pairing in early stages of shear layer mixing.

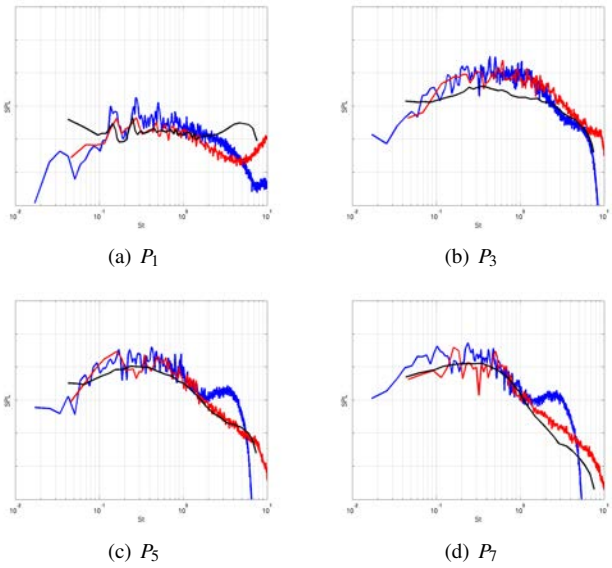

(a) P_1 (b) P_3

(c) P_5 (d) P_7

Figure 9. Comparison of near-field sound for B118. Spacings of SPLs are 10dB. black, experiment; blue, LES(118M); red, LES(118F)

For prediction of far-field noise we employed a noise projection module based on the early work of Ffowcs Williams & Hawkings (1969) and its extension by Spalart & Shur (2009). Figure 4 demonstrates a flow snapshot and the control surface that encloses the sources of sound. Figure 10 shows comparisons of the far-field sound as a function of the microphone stations in figure 5. Far-field sound, is calculated and averaged for 120 equally spaced azimuthal points. Figure 10 shows a comparison between experimental measurements, and computed sound using medium and fine simulations. According to these results, the sound pressure spectra in the fine simulation extends to $St = 10$, while spectra from the medium calculation drops at frequencies beyond $St = 3$. The discrepancy of computed results and experiment at most of the microphone location (except M_8) is approximately 3dB-5dB. One possible source of this discrepancy is the forward flight effect of $M = 0.1$ in experiment which is not accounted for in the FWH computations. A much better agreement is obtained in a different validation study of jet noise (not shown here) where the free-stream mach number is very small. We are currently including the forward-flight effect in the acoustic projection to further understand the sources of the discrepancy.

4 Simulation of an over-expanded heated jet

For this simulation, we used the B118 nozzle designed for $M = 1.5$ and nozzle pressure ratio of $NPR = 3.67$; however, we change the nozzle operating condition to an over-expanded case with $NPR = 2.97$. The temperature ratio for this jet is $T_r = 1.734$.

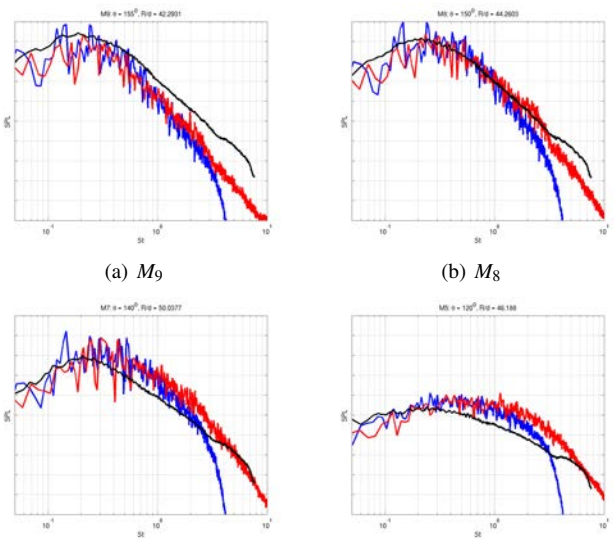

(a) M_9 (b) M_8

(c) M_7 (d) M_5

Figure 10. Comparison of far-field sound for B118. Spacings of SPLs are 5dB. black, experiment; blue, LES(118M); red, LES(118F)

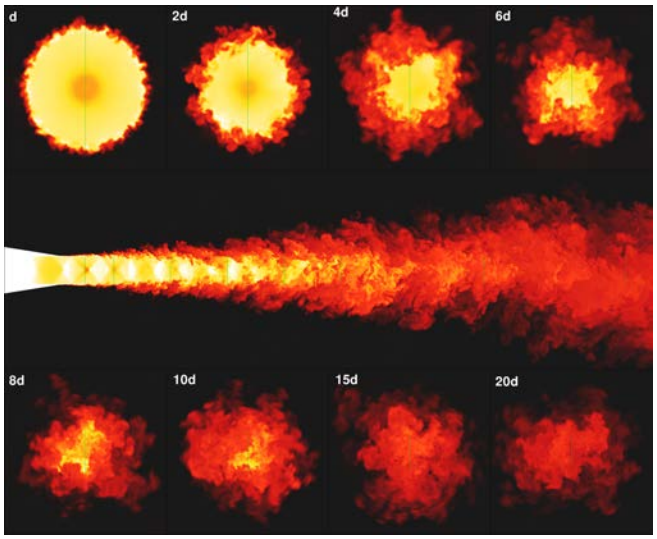

Figure 11. Temperature field for the over-expanded heated jet. The axial cuts of temperature are shown in top and bottom subfigures. The darkest and lightest colors show T_0 and $2T_0$, respectively. T_0 is the atmospheric temperature.

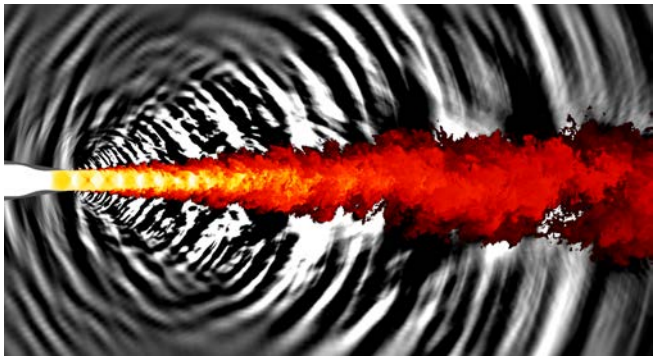

Figure 12. Temperature and pressure field for the over-expanded heated jet shown in redscale and grayscale, respectively.

In contrast to the previous case, strong shocks are present here and the shock capturing scheme described earlier is active in this simulation. Besides the operating conditions and activation of the shock capturing scheme, other simulation parameters including the computational mesh, free-stream flow, time-step size, probe and microphone locations, and sponge zones are identical to simulation parameters corresponding to 118F described above.

Figure 11 demonstrates the instantaneous temperature field and the cuts normal to the axis of the jet; development of turbulent structures from small scale azimuthal structures in the early stages of shear layer till closure of potential core is clearly shown in this figure. In figure 12, the turbulent structures are visualized by showing the contours of temperature (in redscale) and sound is visualized by contours of pressure (in grayscale). Shock cells and fine turbulent structures are clearly visible in this figure. In addition, sound waves emitted to downstream and upstream of the jet are clearly shown. The former is caused by large scale structures while the latter is connected to the interaction of turbulent structures and strong shocks.

Due to the presence of strong shocks, the shock capturing scheme is locally active in the vicinity of the shocks including in the near-nozzle region; however, excessive amount of dissipation introduced by the shock capturing scheme can artificially delay the laminar-turbulent transition of the shear layer issued from the nozzle. The scheme developed within CharLES introduces minimal amount of dissipation by introducing a shock switch (see Section 2). Figure 13 shows a zoom of the shear layer issued from the nozzle. According to this figure, the shear layer instability appears immediately downstream of the nozzle demonstrating the suitability of the shock capturing scheme for this flow. The computational mesh is also included in this figure demonstrating the resolution required to resolve the fine structures in the turbulent shear layer.

The near-field sound spectra computed from this simulation is shown in figure 14. For comparison, the results of the B118 case is also presented in these plots. A tonal component is clearly visible at $St = 0.34$ in sound spectra computed at P_1 and P_3. This tonal component corresponds to jet screech. The broadband shock noise component is also visible in sound spectra at P_3 and P_8 as a broadband peak in the vicinity of $St = 0.7$.

The far-field sound calculation for this case and validation against experiments conducted at UTRC is currently underway

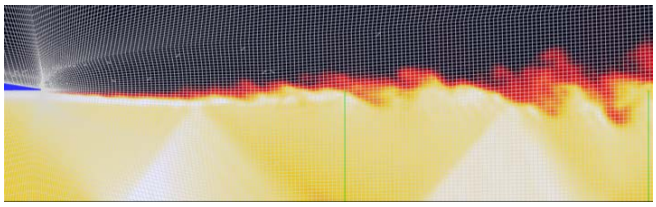

Figure 13. Contours of temperature overlaid on mesh showing the instability of shear layers issued from the nozzle.

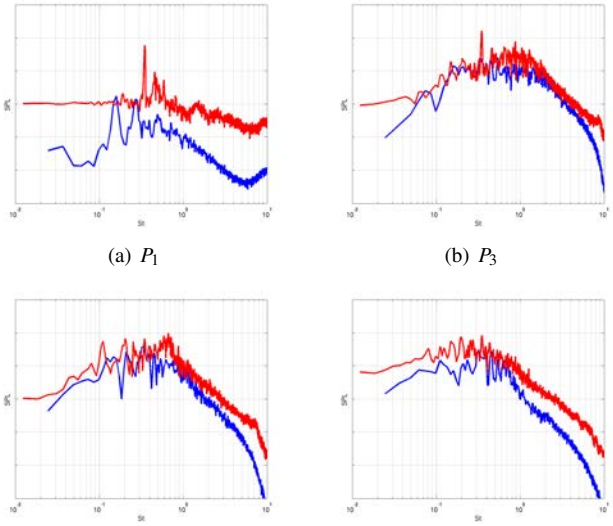

(a) P_1 (b) P_3 (c) P_5 (d) P_7

Figure 14. Near-field sound spectra. Spacings of SPLs are 10dB. red, under-expanded heated jet; blue, ideally-expanded isothermal jet.

and will be presented in future.

5 Pressure-mismatched impinging jets

In this section we present two examples of more complicated supersonic jet configurations. In both examples supersonic pressure mismatched jets interact with obstacles downstream creating a complex flow and sound field; the flow exhibits transition, turbulence and strong shocks. These shocks are generated by over/under-expansion of flow as well as the deceleration of the supersonic jet due to the presence of an obstacle downstream. The examples and limited results are presented here to demonstrated the capability of CharLES. The full details of these simulations and analysis of the results are beyond the scope of the present paper.

5.1 Impinging jet on ground

Combat aircrafts designed for short takeoff and vertical landing (STOVL) achieve their short takeoff by redirecting the propulsive force. During takeoff the propulsive nozzles are rotated downwards towards the ground to create a substantial lift force. The interaction of the jet plume with the ground also introduces additional complexities in the flow field and its aeroacoustic behavior. The hot supersonic jet plume, which typically contains shock-cells impinges on the ground and gets redirected to form a wall-jet, which spreads over the ground. When the jet nozzle is sufficiently close to the ground the plume impingement generates a stand-off shock close to the ground which buffets around as energetic turbulent eddies of the jet plume interact with it. Turbulent eddies in turn get strained and turned to flow along the wall jet. Both processes generate additional intense noise often containing multiple tonal components associated with various feedback loops in the overall flow. The noise generated by the plume/ground interaction radiates in all directions and impinges strongly on the propulsive nozzles and the airframe. When the nozzles are close to the ground there is also a strong aerodynamic interaction creating a suck-down force or thrust loss on the airframe. Depending on the specific configuration the vibro-acoustic loading on the nozzle and airframe components can be substantial.

We reproduced the experiments at the STOVL supersonic facility of the Advanced Aero-Propulsion Laboratory (AAPL) at the Florida State University (Krothapalli *et al.*, 1999). While keeping the geometry constant, we varied the nozzle pressure ratio (NPR) from ideally-expanded condition ($NPR = 3.67$) to extremely under-expanded conditions ($NPR = 10.0$). The stagnation temperature ratio of 1.0 was applied to all the cases. Following the experimental setup Krothapalli *et al.* (1999), a convergind-diverging nozzle is used; the diverging part of the nozzle is a 3^o angle conical shape; the throat diameter is d_t; the nozzle is connected to a circular plate with diameter D, which is parallel at a distance h to a large plate, and the nozzle diameter is d. In this case $D/d_t = 10$ and $H/d_t = 4$. A schematic of this problem is shown in figure 15.

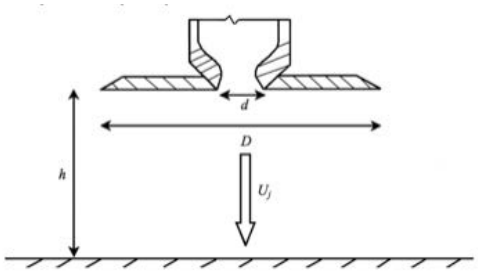

Figure 15. Schematic of the experimental setup taken from Krothapalli *et al.* (1999)

The LES mesh was designed such that the minimum resolution of the mesh supports the maximum frequency of interest (5

KHz) by assuming 5 points/wavelength. This results in a maximum grid size of $\Delta_{max}/d = 0.05$. The minimum resolutions is applied radially within the shear layer $\Delta_r^{min}/d = 0.004$. We improved the mesh by increasing the mesh density in the vicinity of shear layers and also in the impingement region. A planar view of the mesh and cuts normal to the jet axis is demonstrated in figure 16. Instantaneous temperature field is shown with the mesh to demonstrate that the local mesh refinement in the mesh is resolving the turbulent structures. The size of this mesh is 7.7 million. We also carried out a refined calculation of the pressure matched case where the mesh was homothetically refined, The number of cells in the refined mesh is 57 million.

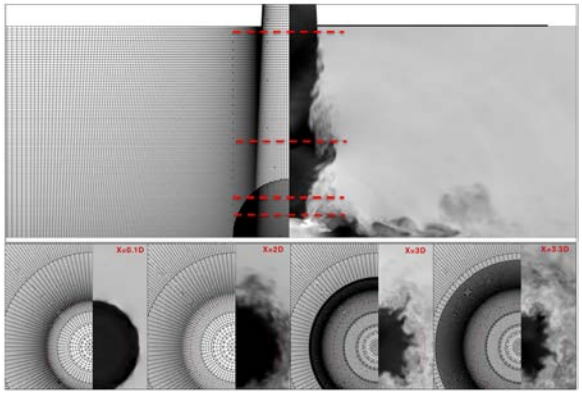

Figure 16. Unstructured mesh and various planar cuts normal to the jet axis.

Instantaneous temperature and pressure contours for nozzle pressure ratios of 3.67 and 10.0 are shown in Figure 17. For the perfectly expanded case at nozzle pressure ratio of 3.67 (shown in figure 17-a) the flow issued from the nozzle is initially laminar; the shear layers go through a transition and at distance of approximately two diameters from the nozzle exit, the jet flow is entirely turbulent. Weak shocks form in the jet plume due to the fact that the divergent part of the nozzle is a straight cone. In the vicinity of the impinging plate a strong stand-off shock is formed that slowly undulate in the vertical direction and the stagnation bubble formed at the impingement "breathes" and interacts with the turbulent shear layer issued from the nozzle. The turbulent structures that pass through the shock are compressed and heated. Note that due to local nature of the shock-capturing scheme, the scheme introduces minimal dissipation and consequently does not destroy the turbulent structures passing through the shock. The turbulent shear layer impinging the ground spread radially and manifest itself as wall jets. According to the pressure contours, the sound is mainly generated by the impingement of the jet. The sound waves travel trough the medium and reflect off the lifting plate and the impinging plate. By increasing the nozzle pressure ratio to 10.0 (see Figure 17-b), a strong shock disk is formed at the nozzle exit; the stand-off shock moves upward and flow within the stagnation bubble appears to recirculate. The sound waves in this case are clearly more energetic than previous configuration. It should be noted that flow snapshots shown in figure 17-a and figure 17-b are taken from the fine (57 M cells) and coarse (7.7 M cells) meshes, respectively. Accordingly, finer turbulence structures are visible in figure 17-a.

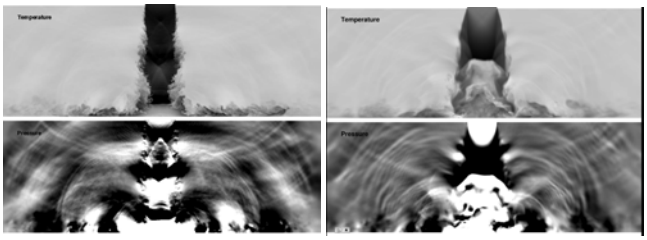

(a) NPR = 3.67 (perfectly-expanded) (b) NPR = 10.0 (under-expanded)

Figure 17. Instantaneous temperature(bottom) and pressure(top) fields for the impinging jet at two nozzle pressure ratios.

We applied a FWH projection method along with method of images to compute the far-field noise; figure 18 compares the sound pressure level from the perfectly-expanded case with the recent experimental measurements of Gustavsson *et al.* (2010) at the same operating condition. The sound was measured at 90^o angle and 13.7 diameters away from nozzle exit. The numerical results are in excellent agreement with the measurements. The shape of the spectra is well predicted and the frequency and the amplitude of the tonal components agree well with the measurements. The numerical results extends to 50 KHz and does not show any sudden drop due to excessive numerical dissipation. The results confirms the predictive capability of the solver and underlying numerical method.

5.2 Impinging jet on a jet blast deflector

The jet blast deflector (JBD) on an aircraft carrier deck is essentially a ramp, which is designed to deflect the propulsive jet plume upwards and help redirect the intense noise away from the ground crew on deck. It creates a shadow zone immediately behind, but its impact on ground personnel in the area upstream of the ramp is not well understood. JBD also redirects the noise around its barrier with increased noise levels on its lateral sides behind it. Optimal shaping of JBD to mitigate the noise exposure to aircraft carrier deck crew can be evaluated with modeling tools, which capture the aeroacoustics of these complex flows.

In this section, we present a "proof of concept" LES of a jet blast deflector. In order to model a realistic nozzle, we assumed that the diverging part of the nozzle is a 3^o angle conical shape

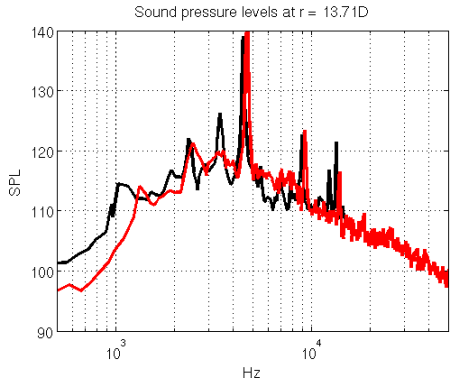

Figure 18. Comparison of sound. red, LES computations and FWH; black, experiment of Gustavsson *et al.* (2010) for perfectly-expanded conditions.

(instead of a nozzle profile designed using method of characteristics); the throat diameter is d; and the exit diameter is d_e. The jet issued from the nozzle impinges on a blast deflector with distance x from the exit. A schematic of this problem is shown in figure 19. The geometry of this configuration was obtained from GE Global Research and the details are given below:

$(d_e/d)^2 = 1.3$
$x/d = 7.5$
$y/d = 2.0$
$L/d = 3.75$
$W/d = 9.8$
$Q = 48^o$
Nozzle tilt angle = 1.8^o (aircraft nose down)

The nozzle is operating at over-expanded conditions with $NPR = 3.75$ and is heated. The static temperature ratio is 5.0.

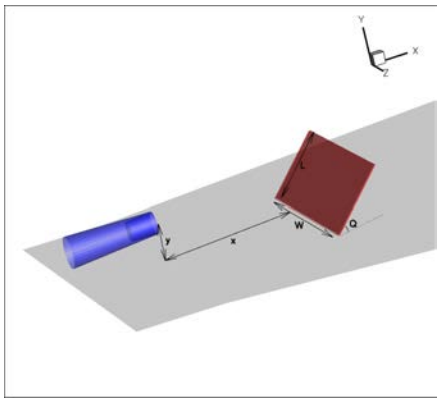

Figure 19. Schematic of a jet blast deflector configuration

We employed an unstructured mesh with local refinement around the nozzle and the blast deflector for this case. The mesh consists of 37 M unstructured elements. An instantaneous flow field obtained from this computation is shown in Figure 20. All the expected features from this flow such as shock cells, turbulent mixing, interaction with the deflector and overspill of the flow are clearly visible in this figure. According to this figure, the sound waves, primarily travel upward; however, the blast deflector does not entirely shield the sound waves and a substantial portion of them travel downstream of the deflector.

In figure 21, 1st- and 2nd-order flow statistics (and derived quantities) are shown. It is clear from figure 21-d that the mesh transition far from the nozzle affects the energy of sound waves.

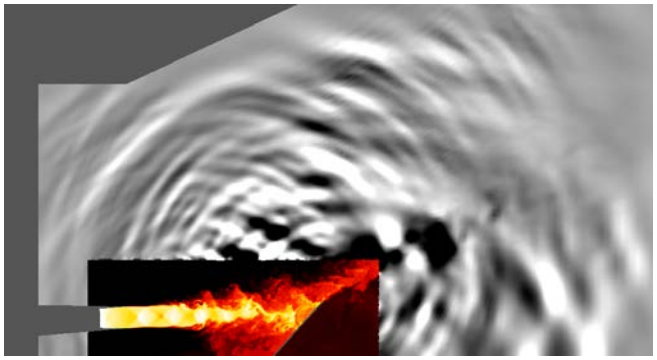

Figure 20. Flow and sound field for a JBD configuration. Contour of instantaneous temperature field is plotted in redsclae. Contour of instantaneous pressure field is plotted in gray-scale.

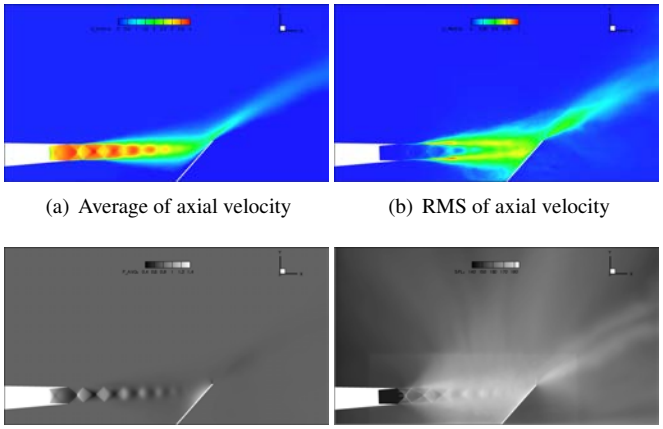

(a) Average of axial velocity (b) RMS of axial velocity

(c) Average of pressure (d) Overall sound pressure level

Figure 21. Low-order statistics computed for the JBD configuration.

6 Summary

In this work we presented a robust and efficient method for the LES of turbulent flows with strong shocks. This method was implemented within Cascade Technologies' unstructured LES code, CharLES. The shock capturing scheme is designed such that dissipation introduced by the scheme minimally affects the turbulence. This method was employed to three under- and over-expanded jets with different levels of complexities. For the case of the free jet, we are currently working on the validation of far-field noise and comparison to the ongoing experiment at UTRC. In addition, we include the results of the fine-resolution simulation of a pressure matched jet as the continuation of our previous effort (Khalighi *et al.*, 2010) to investigate the effect of mesh resolution on predicted flow/sound.

7 Acknowledgement

The authors are thankful to Dr. Joseph Nichols for his contribution in the LES efforts in the paper. The flow condition and geometric configuration of JBD are provided by Dr. Steven Martens from GE global research. This work is supported by NAVAIR STTR program under grant number N68335-07-C-0017 and NAVAIR SBIR program under grant number N68335-10-C-0563.

REFERENCES

BODONY, D. J. & LELE, S. K. 2008 Current status of jet noise predictions using large-eddy simulation. *AIAA J.* **46**, 346–380.

BRIDGES, J. & WERNET, M. P. 2008 Turbulence associated with broadband shock noise in hot jets. In *14th AIAA/CEAS Aeroacoustics Conference, Vancouver, CANADA, 5-7 May 2008*.

FFOWCS WILLIAMS, J. E. & HAWKINGS, D. L. 1969 Sound Generation by Turbulence and Surfaces in Arbitrary Motion. *Royal Society of London Philosophical Transactions Series A* **264**, 321–342.

GUSTAVSSON, J. P. R., RAGALLER, P. A., KUMAR, R. & ALVI, F. S. 2010 Temperature effect on acoustics of supersonic impinging jet. In *16th CEAS/AIAA Aeroacoustics Conference*. Stockholm, Sweden, AIAA paper 2010-3785.

KHALIGHI, Y., HAM, F., MOIN, P., LELE, S. K., COLONIUS, T., SCHLINKER, R. H., REBA, R. A. & SIMONICH, J. 2010 Unstructured large eddy simulation technology for prediction and control of jet noise. In *Proceedings of ASME Turbo Expo 2010: Power for Land, Sea and Air*. Glasgow, UK, GT2010-22306.

KROTHAPALLI, A., RAJKUPERAN, E., ALVI, F. & LOURENCO, L. 1999 Flow field and noise characteristics of a supersonic impinging jet. *Journal of Fluid Mechanics* **392**, 155–181.

LADEINDE, F., CAI, X., ALABI, K., REBA, R., SCHLINKER, R. H. & SIMONICH, J. 2008 On the connection between near-field and far-field solutions of high-speed jet noise. In *AIAA Aerospace Science Meeting*. Reno, AIAA Paper, AIAA-2008-11.

LO, S. C., BLAISDELL, G. A. & LYRINTZIS, A. S. 2008 Numerical simulation of supersonic jet flows and their noise. In *AIAA Aerospace Science Meeting*. Reno, AIAA Paper, AIAA-2008-2970.

MANI, A. 2010 On the reflectivity of sponge zones in compressible flow simulations. *Center for Turbulence Research Annual Research Briefs, Stanford, CA* .

MANI, A., LARSSON, J. & MOIN, P. 2009 Suitability of artificial bulk viscosity for large-eddy simulation of turbulent flows with shocks. *Journal of Computational Physics* **228**, 7368–7374.

NRAC REPORT 2009 Naval research advisory committee report on jet engine noise reduction.

SCHLINKER, R. H., SIMONICH, J. C., REBA, R. A., COLONIUS, T. & LADEINDE, F. 2008 Decomposition of high speed jet noise: Source characteristics and propagation effects. In *14th CEAS/AIAA Aeroacoustics Conference*. Vancouver, British Columbia, AIAA paper 2008-2890.

SHUR, M., SPALART, P., STRELETS, M. & TRAVIN, A. 2003 Towards the prediction of noise from jet engines. *International Journal of Heat and Fluid Flow* **24**, 551–561.

SHUR, M. L., SPALART, P. R. & STRELETS, M. K. 2005 Noise prediction for increasingly complex jets. part i: Methods and tests. *International Journal of Aeroacoustics* **4** (3-4), 213–246.

SPALART, P. R. & SHUR, M. L. 2009 Variants of Ffowcs Williams-Hawkings equation and their coupling for simulation of hot jets. *International Journal of Aeroacoustics* **4** (3-4), 247–266.

TUCKER, P. G. 2004 Novel miles computations for jet flows and noise. *International Journal of Heat and Fluid Flow* **25**, 625–635.

WITZE, P. O. 1974 Centerline velocity decay of compressible free jets. *AIAA J.* **12**, 417–418.

XIA, H., TUCKER, P. G. & EASTWOOD, S. 2009 Large-eddy simulations of chevron jet flows with noise predictions. *International Journal of Heat and Fluid Flow* **30**, 1067–1079.